J. Fluid Mech. (2004), *vol.* 511, *pp.* 45–65.
DOI: 10.1017/S0022112004008559 Printed in the United Kingdom

Survey of instability thresholds of flow between exactly counter-rotating disks

By C. NORE[1,2], M. TARTAR[2], O. DAUBE[3] AND L. S. TUCKERMAN[2]

[1]Université Paris XI, Département de Physique, 91405 Orsay Cedex, France

[2]Laboratoire d'Informatique pour la Mécanique et les Sciences de l'Ingénieur, CNRS, BP 133, 91403 Orsay Cedex, France

[3]LMEE, Université d'Evry Val d'Essonne, 40 rue du Pelvoux, 91020 Evry Cedex, France

(Received 27 March 2003 and in revised form 23 October 2003)

The three-dimensional linear instability of axisymmetric flow between exactly counter-rotating disks is studied numerically. The dynamics are governed by two parameters, the Reynolds number Re based on cylinder radius and disk rotation speed and the height-to-radius ratio Γ. The stability analysis performed for $0.5 \leqslant \Gamma \leqslant 3$ shows that non-axisymmetric modes are dominant and stationary and that the critical azimuthal wavenumber is a decreasing function of Γ. The patterns of the dominant perturbations are analysed and a physical mechanism related to a shear layer instability is discussed. No evidence of complex dynamical behaviour is seen in the neighbourhood of the $1:2$ codimension-two point when the $m = 2$ threshold precedes that of $m = 1$. Axisymmetric instabilities are also calculated; these may be stationary or Hopf bifurcations. Their thresholds are always higher than those of non-axisymmetric modes.

1. Introduction

The flow above a rotating disk and between rotating disks in a cylindrical cavity, or von Kármán swirling flow (Zandbergen & Dijkstra 1987), was first studied by von Kármán (1921) and Batchelor (1951) and occurs frequently in geophysical situations such as atmospherical eddies and in industrial applications such as turbomachines. It depends qualitatively on the height-to-radius aspect ratio Γ, as well as on the ratio s of the angular velocities of the upper and lower disks.

Most studies have focused on the rotor–stator configuration with $s = 0$. For $\Gamma = O(1)$, attention was initially devoted to the possible appearance of axisymmetric recirculation zones on the cylinder axis called vortex breakdown. These bubbles do not seem to result from an instability but rather from a continuous evolution of the basic state. As computational capabilities have increased, interest has turned to the breaking of axisymmetry (e.g. Sotiropoulos & Ventikos 1998, 2001; Spohn, Mory & Hopfinger 1998; Blackburn & Lopez 2000, 2002; Gelfgat, Bar-Yoseph & Solan 2001; Lopez, Marques & Sanchez 2001). Gelfgat, Bar-Yoseph & Solan (2001) performed a linear stability analysis of the steady axisymmetric base flow in the range $\Gamma \in [1, 3.5]$ and found that, for $1.63 \leqslant \Gamma \leqslant 2.76$, the first bifurcation is to an axisymmetric and oscillatory state. Outside this range, the instability is not axisymmetric and azimuthal wavenumbers $m = 2,\ 3$ or 4 dominate.

When $\Gamma \ll 1$ and $s = 0$, the dynamics are dominated by the boundary layer instabilities, namely the Ekman and Bödewadt boundary layers, in the neighbourhood

of the rotating and the stationary disk, respectively (e.g. Schouveiler, Le Gal & Chauve 1998, 2001; Gauthier, Gondret & Rabaud 1999; Serre, Crespo del Arco & Bontoux 2001). Instabilities occur in the form of propagating spirals or circular vortices. These boundary-layer instabilities are of two types (I and II, or B and A) and thought to be related to an unstable inflection point, and to the Coriolis force, respectively. They have been extensively studied, both experimentally and theoretically, within the framework of the self-similar von Kármán equations for flow above a single rotating disk; see e.g. Faller (1991); Pikhtov & Smirnov (1993) and references cited in Schouveiler *et al.* (2001). (Gauthier *et al.* 2002 observed similar patterns in the co-rotating configuration $s > 0$ and in some weakly counter-rotating cases.)

The counter-rotating case $s < 0$ has recently opened a new area of study. In this case, instabilities arise in the free shear layer lying between two regions of opposite azimuthal velocities. Lopez *et al.* (2002) have varied s between 0 and -0.8, for $\Gamma = 0.5$ and $Re = 1000$ and have observed rotating waves in the form of funnel-like vortices with azimuthal wavenumbers 4 and 5, as well as more complicated dynamics. For $\Gamma \sim 0.05$, Gauthier *et al.* (2002) also observed a new pattern of spirals, which roll up towards the centre in the direction opposite to that of the faster disk. They suggested that this spiral structure is engendered by the same free shear layer instability as in Lopez *et al.* (2002). Moisy *et al.* (2003) confirmed this hypothesis with an experimental study in the range $\Gamma \in [1/20.9, 1/3.8]$ and $s \in [-1, -0.135]$, in which the pattern consists of vertical vortices surrounded by these negative spirals. At moderate Γ and/or large Reynolds numbers, the vortices are preferred while, at small Γ and/or small Re, the negative spirals dominate.

In a previous paper (Nore *et al.* 2003), we have studied the exactly counter-rotating case, $s = -1$, at a fixed aspect ratio $\Gamma = 2$. We have shown that, when the disk rotation rate is increased, the axisymmetric basic state becomes unstable through a Kelvin–Helmholtz instability of the equatorial azimuthal free shear layer created by the counter-rotation of the top and bottom disks. This instability gives rise to steady states with one or two radially oriented vortices and is accompanied by more complex dynamics like travelling waves, modulated travelling waves, and near-heteroclinic cycles.

The main purpose of this paper is to study the linear threshold of the order parameter, the Reynolds number, when varying the aspect ratio Γ and keeping $s = -1$, i.e. the bottom and top disks are exactly counter-rotating. The outline of the paper is as follows: in § 2, the problem is formulated, along with its symmetries; § 3 summarizes the numerical methods and code validation. In § 4.1, the non-axisymmetric thresholds for bifurcations from the basic axisymmetric state are reported, together with the patterns of the eigenvectors. The physical mechanism is interpreted in § 4.2 as a manifestation of the Kelvin–Helmholtz instability as previously suggested in Nore *et al.* (2003). In § 4.3, we investigate the nonlinear behaviour of the azimuthal modes $m = 2$ and $m = 1$ near their codimension-two point, in light of the complex dynamical states observed in Nore *et al.* (2003). The axisymmetric thresholds are studied in § 5 although the $m = 0$ mode is never the most unstable: up to two real and two complex eigenvalues interact, leading to a variety of different bifurcations. Section 6 contains our conclusion.

2. Formulation of the problem

2.1. *The governing equations*

We consider a cylindrical cavity of radius R and height H filled with an incompressible fluid of kinematic viscosity ν and density $\rho = 1$. The motion is driven by the upper

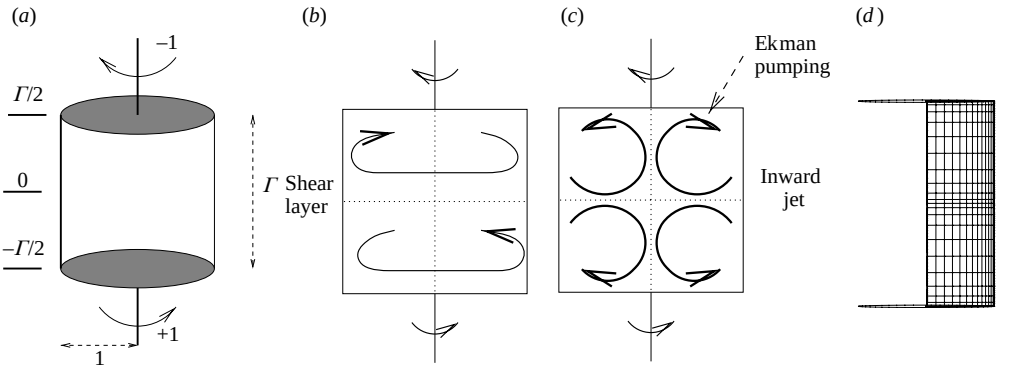

FIGURE 1. (*a*) Sketch of the flow geometry in non-dimensionalized units. (*b*) Equatorial shear layer separating two regions of opposite azimuthal velocities. (*c*) Recirculation zones due to Ekman pumping meet, forming a radially inward jet. (*d*) The non-uniform grid in the (r, z)-plane used for computations at $\Gamma = 3$. For clarity, only one out of five points is represented in each direction.

and lower disks rotating at constant angular velocity Ω_{up} and Ω_{low}, respectively. The dimensionless momentum and continuity equations read

$$\frac{\partial \boldsymbol{v}}{\partial t} + (\boldsymbol{v}\cdot\nabla)\boldsymbol{v} = -\nabla p + \frac{1}{Re}\nabla^2\boldsymbol{v}, \tag{2.1a}$$

$$\nabla\cdot\boldsymbol{v} = 0, \tag{2.1b}$$

where $\boldsymbol{v}$ is the velocity, p the pressure, and $Re = \Omega_{low}R^2/\nu$ the Reynolds number. The velocity, pressure, length and time are non-dimensionalized by $\Omega_{low}R$, $\rho(\Omega_{low}R)^2$, R and $1/(2\pi\Omega_{low})$ (the rotation period), respectively. Two supplementary non-dimensional parameters are the aspect ratio $\Gamma = H/R$ and the angular velocity ratio $s = \Omega_{up}/\Omega_{low}$. We study the case where the disks rotate at exactly opposite angular velocities, namely $s = -1$, and vary the aspect ratio. The flow geometry is sketched in figure 1(*a*).

The boundary conditions on the cylinder walls are:

$$\boldsymbol{v} = 0 \qquad \text{on the stationary sidewall at } r = 1, \tag{2.2a}$$

$$\boldsymbol{v} = \pm r\boldsymbol{e}_\theta \qquad \text{on the rotating disks at } z = \mp\Gamma/2. \tag{2.2b}$$

2.2. *Symmetries*

Figure 1 depicts the basic axisymmetric steady flow, which consists of a predominant equatorial shear layer produced by the counter-rotating lower and upper disks and separating two regions with opposite senses of azimuthal velocities. Two second-order recirculation zones due to Ekman pumping in the neighbourhood of each disk (figure 1*c*) converge at mid-height and form an inward radial jet.

The geometry and basic state are axisymmetric and thus invariant under rotations S_{θ_0} by angle θ_0 about the z-axis. The case $s \equiv \Omega_{up}/\Omega_{low} = -1$ admits a supplementary symmetry of rotation of π about any horizontal axis, for example the x-axis, which we denote by R_π. This rotation is equivalent to combined reflections in $\theta = 0$ and in $z = 0$. R_π does not commute with S_{θ_0} and hence, the group generated by these operators is isomorphic to $O(2)$.

3. Numerical methods

Our primary goal is to carry out a linear stability analysis of the counter-rotating disk system for a range of aspect ratios. For this purpose, we have used a number of different computational techniques: a steady-state solver, linearized integration about a steady state, the ARPACK library (Lehoucq, Sorensen & Yang 1998) to compute leading eigenvalues and a nonlinear non-axisymmetric code. The main features of these tools are summarized here. Further details can be found in Gadoin, Le Quéré & Daube (2001); Daube & Le Quéré (2002); Barbosa & Daube (2002) and Nore *et al.* (2003).

3.1. *Spatial discretization*

The flow fields are represented in cylindrical coordinates (r, θ, z). Fourier expansions are used in the θ-direction while a staggered non-uniform grid with N_r+1 and N_z+1 gridpoints is used in the (r, z)-plane. The grid is refined at the top, bottom and lateral boundaries and at the mid-plane as shown in figure 1(d) by placing gridpoints at:

$$r_i = \frac{\tanh(\beta i/N_r)}{\tanh(\beta)} \quad (i = 0, \ldots, N_r), \tag{3.1a}$$

$$z_j = \frac{1}{4}\Gamma\left(\frac{\tanh(\beta(2j - N_z/2)/(N_z/2))}{\tanh(\beta)} + 1\right) \quad (j = 0, \ldots, N_z/2), \tag{3.1b}$$

where $\beta = 1.5$. Equation (3.1b) is symmetrized under reflection in the mid-plane for the vertical gridpoints. The only unknown located on the axis $r = 0$ is the axial component of the vorticity. The spatial discretization of the Navier–Stokes equations (2.1) uses mimetic finite-difference operators (Hyman & Shashkov 1997) and is an extension to non-uniform grids of the method described in Barbosa & Daube (2002).

Alongside the upper disk, at the points $z = (z_{N_z/2} + z_{N_z/2-1})/2$, $r < 1$ where v_θ is computed, it is nearly $-r\Omega$ and rapidly attains 0 at the shroud $r = 1$. A numerical gap can be defined as the distance δ over which $|v_\theta|$ attains half its maximum value. With our usual numerical treatment, $\delta \simeq 0.0015$ for $\Gamma = 0.5$. To measure the influence of the junction singularity, we have also imposed a regularized boundary condition consisting of linearly interpolating v_θ between $\pm r\Omega$ at r_{N_r-3} and 0 at r_{N_r}. The resulting gap is $\delta \simeq 0.0038$ and the linear thresholds of azimuthal modes $m = 3, 4, 5$ differ by less than 0.03% from the non-regularized thresholds.

3.2. *Axisymmetric steady states*

Axisymmetric base flows are represented by the azimuthal velocity v and a streamfunction ψ defining the radial and vertical velocities via $\nabla\psi \times \boldsymbol{e}_\theta/r$. Temporal integration is first carried out to obtain a steady state at a low Reynolds number for which the basic axisymmetric state is stable. A Newton–Raphson method is used to calculate states at higher Reynolds numbers, which may be unstable to axisymmetric perturbations. In order to solve the large linear systems involved, we have used the Stokes preconditioned Newton method proposed in Tuckerman (1989) and Mamun & Tuckerman (1995), together with a matrix-free method, such as GMRES (Saad & Schultz 1986). This preconditioned Newton method is very effective, provided that the full discrete coupled system is solved at each time step, rather than relying on approximations whose errors are proportional to some power of the time step Δt. Here, this is achieved by using an influence matrix technique in order to enforce the no-slip condition.

	Resolution		Modes			
	N_r	N_z	0	1	2	3
Thresholds: present code	64	100	2699	3202	2526	3116
Gelfgat *et al.* (2001)	30	30	2724	3217	2523	3119
Frequencies: present code	64	100	0.237	0.497	~ 0	0.111
Gelfgat *et al.* (2001)	30	30	0.2368	0.4949	0.0031	0.1104

TABLE 1. Thresholds and critical frequencies for azimuthal modes $m = 0$ to 3 for a rotor–stator flow $s = 0$ with $\Gamma = 1.5$.

3.3. *Linear stability analysis and time integration*

A non-axisymmetric code using primitive variables carries out both linear stability analysis and nonlinear time integration. The velocity components and pressure are expanded in truncated Fourier series over N_θ modes in the azimuthal direction. Linear stability analysis of a previously computed axisymmetric steady state $\boldsymbol{V}$ is performed by time integration of the linearized Navier–Stokes equations:

$$\frac{\partial \boldsymbol{v}}{\partial t} + (\boldsymbol{V}\cdot\nabla)\boldsymbol{v} + (\boldsymbol{v}\cdot\nabla)\boldsymbol{V} = -\nabla p + \frac{1}{Re}\nabla^2\boldsymbol{v}, \tag{3.2a}$$

$$\nabla\cdot\boldsymbol{v} = 0, \tag{3.2b}$$

where homogeneous boundary conditions are imposed on $\boldsymbol{v}$. The temporal evolution of (2.1) or (3.2) is computed by a second-order implicit discretization of the linear terms and explicit Adams–Bashforth type extrapolation of the nonlinear terms (or their linearized version). The velocity–pressure coupling is handled by means of an incremental projection method (Goda 1979; Daube & Le Quéré 2002).

For an axisymmetric basic state, the stability computation separates into a family of decoupled subproblems each associated with an azimuthal wavenumber m. Therefore linearized time-integration from an arbitrary initial condition corresponds to computing N_θ integrations in parallel. The leading eigenvalues are extracted as half the slope of the evolution under (3.2) of the logarithm of the energy corresponding to each azimuthal wavenumber m. When needed, a limited number of leading eigenvalues of the linearized equations are computed by means of ARPACK, a software package based on an implicitly restarted Arnoldi method (Sorensen 1992; Lehoucq *et al.* 1998).

The procedure is as follows. For a fixed aspect ratio Γ, a stable steady state at $Re^0 = 100$ is computed using the axisymmetric temporal code. Successive axisymmetric steady states at $Re = Re^0 + \Delta Re$ are calculated via Newton's method. These steady states are substituted into the linearized Navier–Stokes equations (3.2), yielding the leading eigenvalue $\lambda(m, Re, \Gamma) = \lambda_r(m, Re, \Gamma) + \mathrm{i}\lambda_i(m, Re, \Gamma)$ for each azimuthal wavenumber $m \leqslant N_\theta/2 - 1$. The neutral Reynolds numbers $Re_m(\Gamma)$ satisfy $\lambda_r(m, Re_m(\Gamma), \Gamma) = 0$ and are determined by interpolation The critical Reynolds number of the flow for each Γ is $Re_C(\Gamma) \equiv min_m Re_m(\Gamma)$. The value of m corresponding to $Re_C(\Gamma)$ is the critical mode m_C.

3.4. *Code validation and resolution*

Our code was tested by comparing our linearized computations with those by Gelfgat *et al.* (2001) for the rotor–stator case $s = 0$ and $\Gamma = 1.5$. Table 1 compares the thresholds and critical frequencies obtained with the resolution $N_r = 64$, $N_z = 100$ to

		Resolution		Modes					
Γ	Grid	N_r	N_z	0	1	2	3	4	5
1.0	Uniform	100	100	1332	420	299	312	387	533
1.0	Non-uniform	64	100	1316	420	300	312	387	534
1.5	Uniform	100	150	1607	332	309	426	653	892
1.5	Non-uniform	64	100	1540	331	309	427	654	893
2.0	Uniform	100	200	1852	349	400	625	909	1205
2.0	Non-uniform	64	100	1842	349	401	625	910	1209
3.0	Non-uniform	32	50	1929	495	647	1019	1427	1869
3.0	Non-uniform	64	100	2156	504	656	1037	1441	1866
3.0	Non-uniform	128	200	2172	507	659	1044	1449	1874

TABLE 2. Thresholds for azimuthal modes $m = 0$ to 5 computed with uniform and non-uniform grids and with different resolutions for the counter-rotating disks $s = -1$.

those calculated by Gelfgat *et al.* (2001) using spectral methods with 30×30 basis functions which are linear superpositions of Chebychev polynomials. Our results agree to within 1% for the thresholds and within 0.5% for the frequencies.

We have performed convergence tests for $s = -1$ and the tallest cylinder under investigation $\Gamma = 3$ with three different resolutions. Results are reported in table 2. In this case, the resolution 64×100 represents a compromise between accuracy and CPU time leading to errors in the thresholds of less than 0.7% for any wavenumber when compared with those of the finest mesh (128×200).

We have also compared the thresholds for three different aspect ratios obtained with the non-uniform grid (3.1) with those obtained using the uniform grid used in Nore *et al.* (2003). For the non-uniform grid, the same number of gridpoints is used for all aspect ratios, while for the uniform grid, the number of vertical gridpoints N_z is varied proportionately to the aspect ratio. For each aspect ratio, table 2 shows that the differences are less than 0.5%, except for the $m = 0$ mode. The difficulty in resolving the $m = 0$ instability is confirmed by a comparison with Gelfgat, Bar-Yoseph & Solan (1996), who found $Re_0(\Gamma = 1.5) = 1644$ using an axisymmetric spectral code with 40×40 basis functions, leading to a difference of 6.3% compared with our $m = 0$ result for the resolution 64×100. In § 5, we will explain that the largest errors are located at values of Γ at which $Re_0(\Gamma)$ undergoes very rapid change and that the seemingly large size of the error is in fact due to this effect. We will also compare the $m = 0$ thresholds obtained with the temporal linear code and with ARPACK.

The results presented in this paper span the aspect ratio interval [0.5, 3]. For $\Gamma = H/R < 1$, we use more radial than vertical gridpoints and vice versa for $\Gamma \geqslant 1$. More specifically, for $1 \leqslant m \leqslant 5$, computations are performed with $N_r = 100$, $N_\theta = 12$, $N_z = 64$ for $\Gamma < 1$ and with $N_r = 64$, $N_\theta = 12$, $N_z = 100$ for $\Gamma \geqslant 1$. For $m = 0$, we have used an axisymmetric version of the non-uniform code with $N_r = 200$, $N_z = 128$ for $\Gamma < 1$ and with $N_r = 128$, $N_z = 200$ for $\Gamma \geqslant 1$. The time step is $\Delta t = 10^{-2}$ non-dimensional time units for $Re < 1000$ and $\Delta t = 0.5 \times 10^{-2}$ for $Re \geqslant 1000$. A typical linear run of 50 disk rotations takes 500 s on a NEC-SX5 computer. About 30 linear runs are necessary to obtain the six thresholds for a fixed aspect ratio. Throughout the paper, we report thresholds as integer values of the Reynolds number.

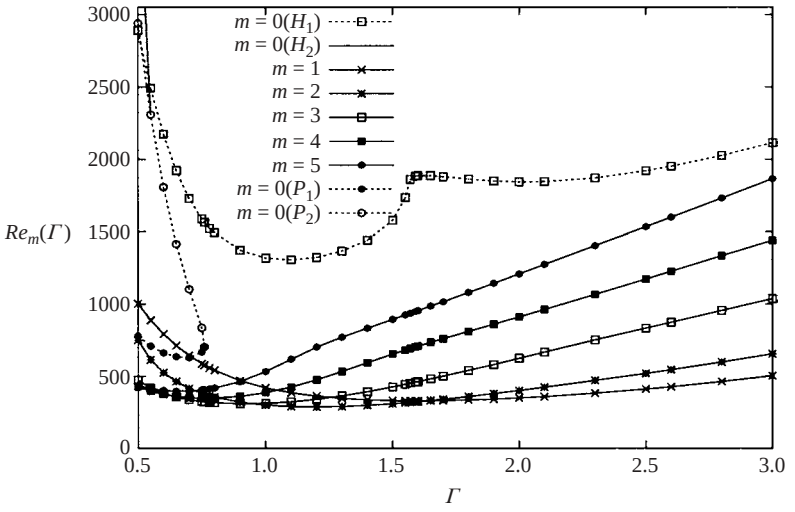

FIGURE 2. Thresholds $Re_m(\Gamma)$ for azimuthal modes $m = 0$ to 5 as functions of the aspect ratio Γ. The modes $m = 1$ to 5 are stationary whereas the $m = 0$ mode is stationary for $m = 0$ (P_1) and (P_2) and oscillatory for $m = 0$ (H_1) and (H_2).

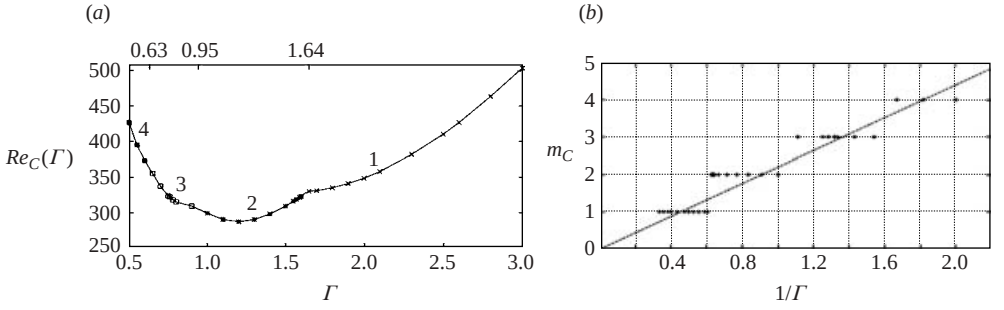

FIGURE 3. (*a*) Critical Reynolds number $Re_C(\Gamma)$ as a function of Γ realized for different critical wavenumbers: ×, $m = 1$; *, $m = 2$; □, $m = 3$; ■, $m = 4$. (*b*) Critical wavenumber m_C (+) as a function of the inverse of Γ with the indicative dashed line $2.2/\Gamma$.

4. Three-dimensional modes

4.1. *Thresholds and eigenvectors*

We study the stability of the flow produced by counter-rotation of the bottom and top disks as a function of the aspect ratio in the range $0.5 \leqslant \Gamma \leqslant 3$. At each Γ, we compute the neutral Reynolds number given by $Re_m(\Gamma)$ for integer values of the azimuthal wavenumber $0 \leqslant m \leqslant 5$ (figure 2). All modes are stationary, i.e. the eigenvalues are zero at threshold, except for those on the branches denoted $m = 0$ (H_1) and $m = 0$ (H_2). The critical Reynolds number $Re_C(\Gamma)$ is the lowest $Re_m(\Gamma)$, minimized over all m, and the corresponding azimuthal mode m_C is the most unstable mode. In the aspect ratio interval under consideration, the axisymmetric mode is never critical and its features differ substantially from those of the non-axisymmetric modes. We therefore begin by describing the $m \neq 0$ mode results and defer description of the $m = 0$ modes and thresholds to a separate section.

Figure 3(*a*) shows $Re_C(\Gamma)$, a lower envelope for the curves $Re_m(\Gamma)$, which yields the lowest threshold for each Γ. The critical Reynolds number $Re_C(\Gamma)$ reaches its

Wavenumber pair	Γ	Re
(4, 3)	0.63	365
(3, 2)	0.95	310
(2, 1)	1.64	330

TABLE 3. Codimension-two points at which two azimuthal wavenumbers compete.

minimum value of 287 for $\Gamma = 1.2$ and $m = 2$. The codimension-two points at which different azimuthal wavenumbers compete are shown in table 3.

The critical azimuthal mode m_C decreases with Γ or, equivalently, increases with $1/\Gamma$. This is seen in figure 3(b), where the line $m = 2.2R/H = 2.2/\Gamma$ has been drawn as a guide. We can observe that $m_C \sim 1 + [2/\Gamma]$ where $[\cdot]$ is the integer part of a real number. This scaling for the first instability was proposed in Nore *et al.* (2003) where it was postulated that the instability is located in the equatorial azimuthal shear layer occupying a constant proportion of the height, leading to an azimuthal wavelength which is half the height.

To illustrate the three-dimensional patterns corresponding to the thresholds in figure 2 we choose four representative cases, with increasing critical wavenumbers $m = 1, 2, 3, 4$. For each case, we show contours of azimuthal velocity v and meridional vector field (u, w) of the unperturbed basic state and of the critical eigenvector. Isosurfaces of the perturbed velocity (u, v, w), contours of w and unfolded contours of radial vorticity illustrate the azimuthal spatial distribution of the eigenvector.

As explained in § 2.2, the symmetry group of the counter-rotating disk system is isomorphic to $O(2)$. Each non-axisymmetric eigenmode is associated with a circle pitchfork bifurcation, producing a circle of steady states parameterized by angular phase θ_0. Each eigenmode possesses a horizontal axis of symmetry; its orientation can be chosen so as to make the eigenmode symmetric under R_π. We illustrate this with figure 4(d), which shows vertical velocity contours of the $m = 1$ eigenvector for $\Gamma = 3$ at $Re = 510$, slightly above the bifurcation threshold $Re_C = 504$. At $z = 0$, the negative contours for $0 < \theta < \pi$ correspond to the positive contours for $\pi < \theta < 2\pi$. The action of R_π relating contours at $z = \Gamma/4$ and $z = -\Gamma/4$ needs more work: choose a feature in the $(\Gamma/4)$-plane, reflect it in θ, take its opposite sign, and find it in the $(-\Gamma/4)$-plane.

Another feature shared by all the eigenmodes is the equatorial location of the maximum disturbance. The isosurfaces (figures 4c, 5c, 6c, 7c) lead to the conclusion that the radial localization evolves with the aspect ratio: for large Γ, the maximum disturbance is located near the vertical axis while, for small Γ, the largest gradients are concentrated at the periphery and are diffused by viscosity in the central region. As Γ decreases, the vorticity changes from helicoidal patterns to two families of spirals, one in each half from the equatorial plane. The spiral arms are directed in the sense of rotation of the nearest disk, preserving the R_π symmetry.

4.2. *Kelvin–Helmholtz mechanism*

The radial vorticity of figures 4(e), 5(e), 6(e) and 7(e) resembles the disturbance that leads to the formation of co-rotating vortices, sometimes called cat's eyes, seen in the Kelvin–Helmholtz instability of a constant-vorticity shear layer. The number of vortices is the azimuthal critical wavenumber. Our observation of vortical structures

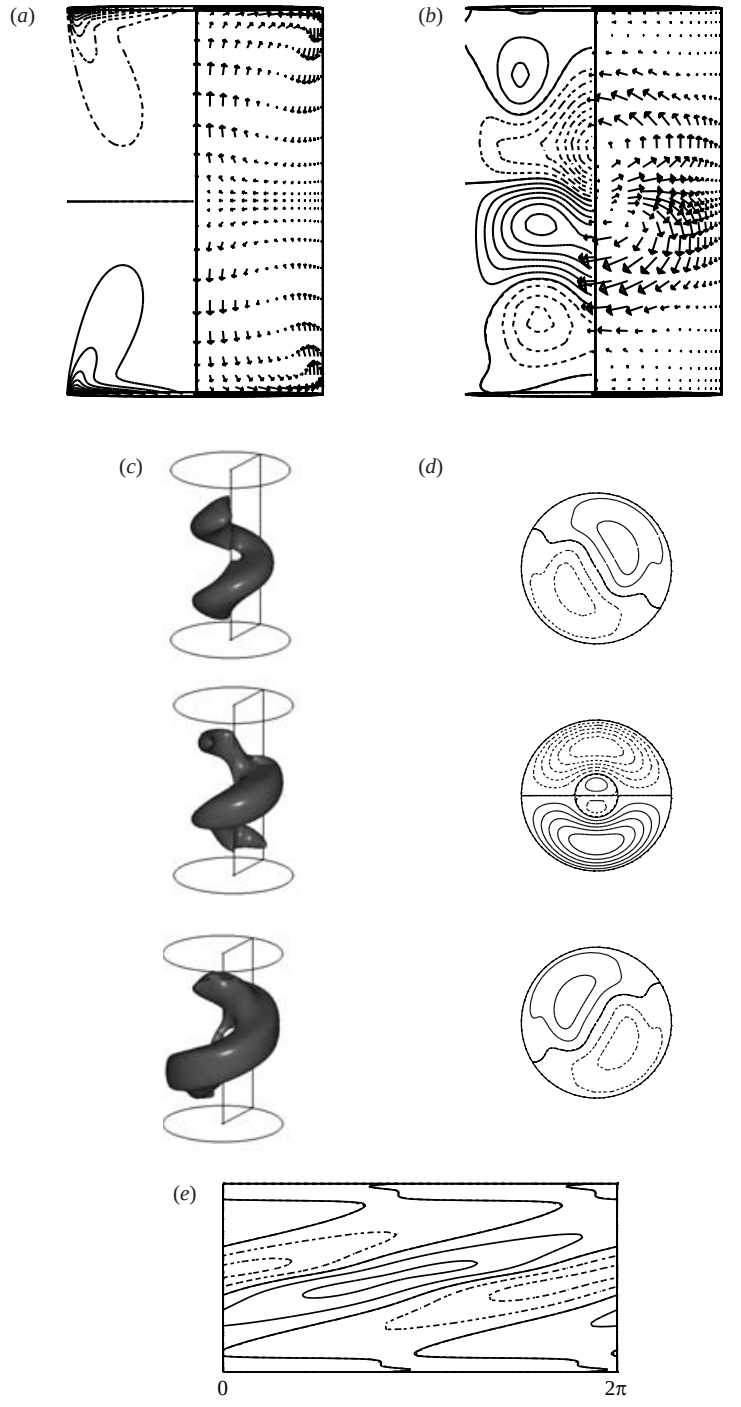

FIGURE 4. The $m=1$ eigenvector for $\Gamma=3$ and $Re=510$. (*a*) Vector field with radial and vertical velocity components (u, w) at $\theta=0$ and contours of azimuthal velocity v at $\theta=\pi$ for the basic state for comparison. (*b*) Vector field (u, w) at $\theta_1=24^\circ$ and contours of v at $\theta_2=\pi+24^\circ$ for the $m=1$ eigenvector. (*c*) Isosurface of u, v and w at a quarter of the maximum positive value viewed slightly from above. (*d*) Vertical velocity contours at $z=\Gamma/4$ (top), $z=0$ (middle), and $z=-\Gamma/4$ (bottom) viewed from above. (*e*) Unfolded radial vorticity contours at $r=0.8$. Positive (negative) values of a scalar function are indicated by solid (dashed) curves.

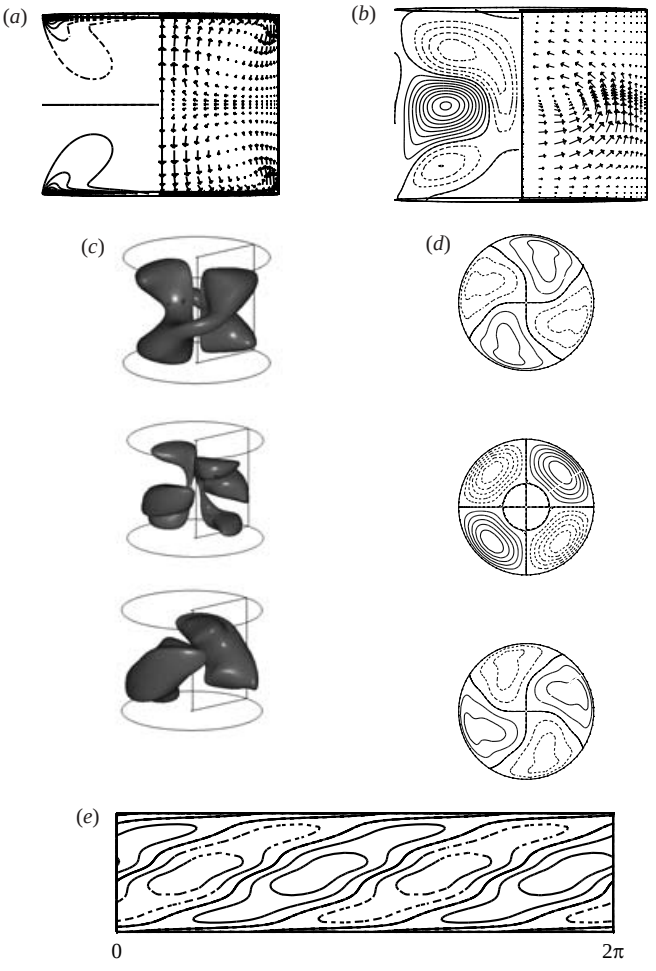

FIGURE 5. The $m=2$ eigenvector for $\Gamma=1.5$ and $Re=320$. Same views as in figure 4, except (*b*) $\theta_1=30^\circ$ and $\theta_2=\pi+30^\circ$ and (*e*) $r=0.81$.

motivates us to extend our interpretation of the instability of the basic axisymmetric flow as a manifestation of the Kelvin–Helmholtz instability (Nore *et al.* 2003).

The Kelvin–Helmholtz instability is a two-dimensional instability of a basic velocity profile $u(y)\boldsymbol{e}_{\mathbf{x}}$ to perturbative modes $(u'(y)\boldsymbol{e}_{\mathbf{x}}+v'(y)\boldsymbol{e}_{\mathbf{y}})\mathrm{e}^{\mathrm{i}\alpha x}$. Betchov & Szewczyk (1963) studied the instability of the standard shear-layer profile $u(y)=U\tanh(y/\delta)$. They computed the marginal stability curve in the $(Re_{\mathrm{KH}},\alpha)$-plane, where $Re_{\mathrm{KH}}=U\delta/\nu$ and $\alpha=2\pi\delta/\lambda$ with λ the wavelength.

In our case, the basic profile is of the form $v(r,z)\boldsymbol{e}_\theta$ and is perturbed by eigenmodes such as $(v'(r,z)\boldsymbol{e}_\theta+w'(r,z)\boldsymbol{e}_z)\mathrm{e}^{\mathrm{i}m\theta}$. The radial dependence is assumed to be weak and then treated as parametric. We fit the central portion of each basic state for the four cases of figures 4, 5, 6 and 7 with a hyperbolic tangent function $v(r,z)/r=\omega(r)\ \tanh(z/\delta(r))$. For example, in figure 8(*a*), for $0.1\lesssim r\lesssim 0.6$, the profiles present vertical tangents at $z\approx\pm 0.7$ and we apply the fit between these values. von Kármán (1921) and Batchelor (1951) derived a velocity profile for the axisymmetric flow between disks of infinite radii for which $v(r,z)/r$ is independent of r. We have verified that this is approximately verified for r between 0.1 and 0.6 at $\Gamma=3$; in

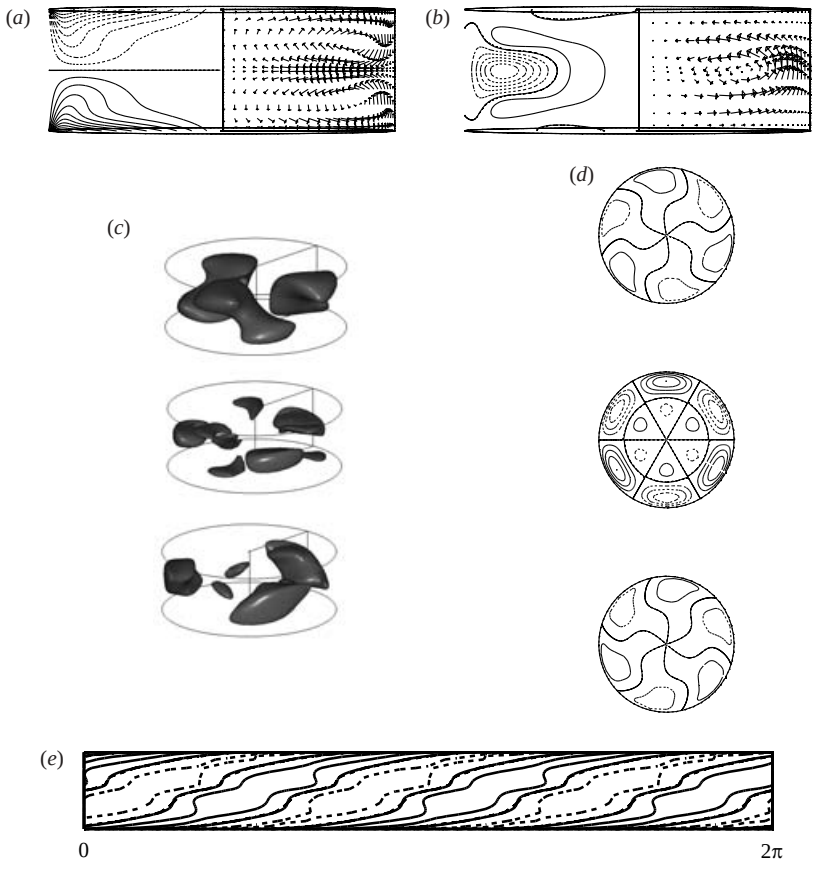

FIGURE 6. The $m = 3$ eigenvector for $\Gamma = 0.7$ and $Re = 340$. Same views as in figure 4, except (*b*) $\theta_1 = -33^\circ$ and $\theta_2 = \pi - 33^\circ$ and (*e*) $r = 0.9$.

particular, $\omega(r)$ and $\delta(r)$ both remain close to 0.3. See also figure 27 of Nore *et al.* (2003) and Cousin-Rittemard, Daube & Le Quéré (1998).

We extend the analysis of Betchov & Szewczyk (1963) to Re_{KH} and α depending on r, and a wavelength which is quantized by the finite circumference of the cylinder. We define

$$Re_{\mathrm{KH}}(r) = r\omega(r)\delta(r)Re, \quad \alpha(r) = \delta(r)m/r, \tag{4.1}$$

with $\nu = 1/Re$ in our units and $2\pi r/m$ the circumferential wavelength corresponding to azimuthal wavenumber m at a radius r. We calculate $\omega(r)$ and $\delta(r)$ for the basic axisymmetric velocity fields at a Reynolds number slightly above threshold for $\Gamma = 3$, 1.5, 0.7 and 0.5 for which the critical wavenumbers are 1, 2, 3 and 4, respectively. We then compute $Re_{\mathrm{KH}}(r)$ and $\alpha(r)$ via (4.1). In figure 8(*b*), we plot these points together with the marginal stability curve of Betchov & Szewczyk (1963); the Kelvin–Helmholtz unstable region is below this curve. It can be seen that, for each aspect ratio, the curve $(Re_{\mathrm{KH}}(r), \alpha(r))$ lies near or inside the Kelvin–Helmholtz unstable region for a radial interval depending on Γ. This analysis provides evidence that the mechanism responsible for the non-axisymmetric instabilities we have calculated is the Kelvin–Helmholtz instability.

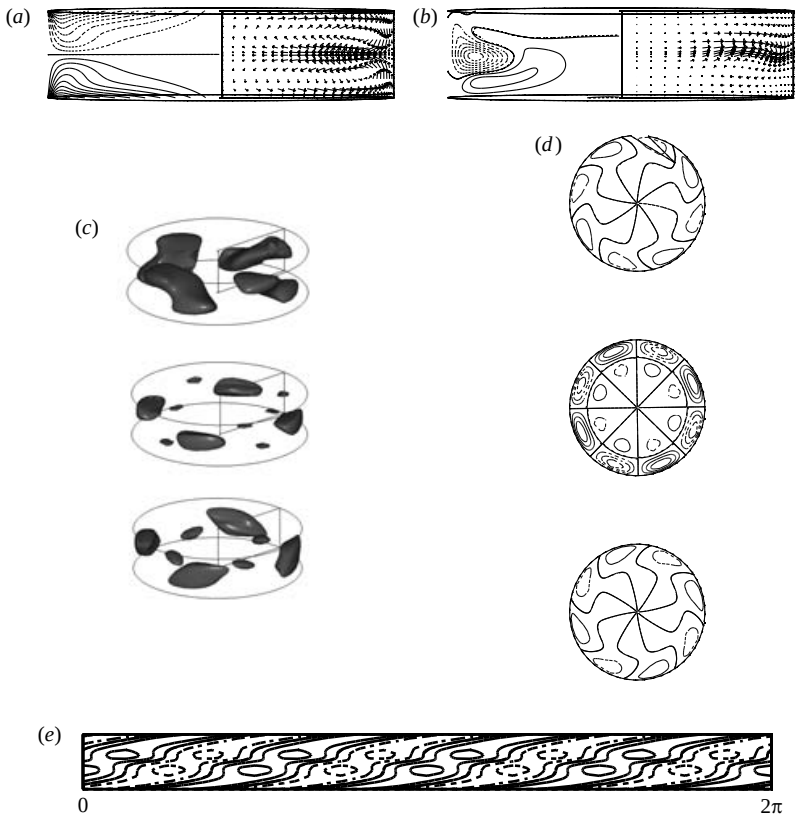

FIGURE 7. The $m = 4$ eigenvector for $\Gamma = 0.5$ and $Re = 430$. Same views as in figure 4, except (*b*) $\theta_1 = -13^\circ$ and $\theta_2 = \pi - 13^\circ$ and (*e*) $r = 0.9$.

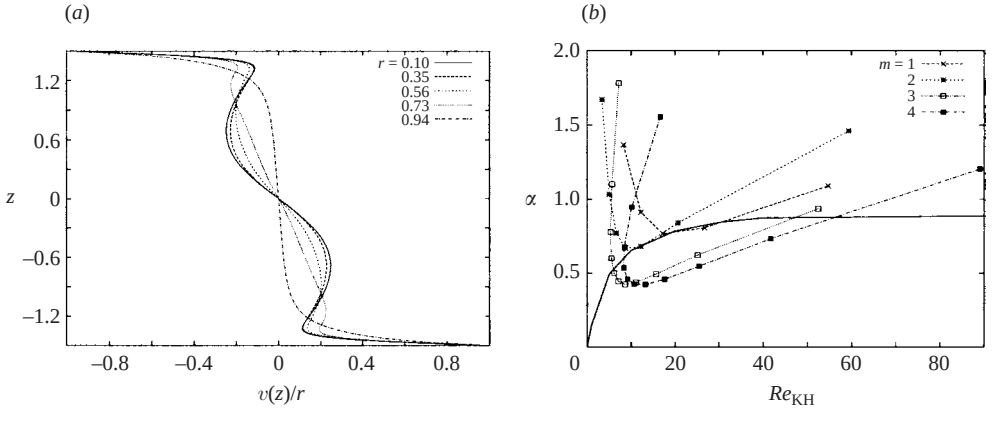

FIGURE 8. (*a*) Azimuthal profiles $v(r, z)/r$ of the axisymmetric basic state for $\Gamma = 3$ at $Re = 510$ above the threshold $Re_{m=1}(\Gamma = 3) = 504$ at different radii as indicated. The similarity zone, defined as the region in which the profiles $v(r, z)/r$ depend only slightly on r, extends from $r \sim 0.1$ to $r \sim 0.6$. (*b*) Wavenumber α (in units of the inverse shear layer thickness) as a function of Re_{KH} computed for $(m, \Gamma, Re) = (1, 3, 510)$, $(m, \Gamma, Re) = (2, 1.5, 320)$, $(m, \Gamma, Re) = (3, 0.7, 340)$, and $(m, \Gamma, Re) = (4, 0.5, 430)$, just above their respective instability thresholds. For $m = 1$, 2, 3 and 4, the r values shown are in the ranges [0.23, 0.65], [0.23, 0.80], [0.38, 0.89] and [0.52, 0.94], respectively, with r increasing from the left to the right endpoint of each curve. The marginal stability calculation of Betchov & Szewczyk (1963) is shown as the solid curve.

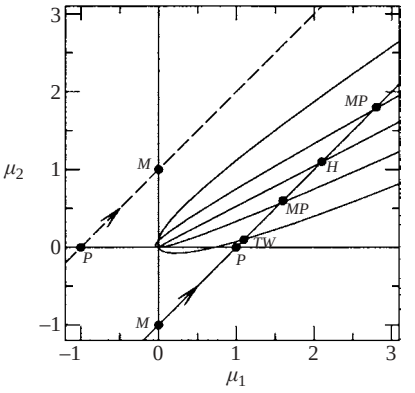

FIGURE 9. Phase diagram near the 1 : 2 codimension-two point. The two trajectories schematically represent increasing Re at two fixed values of Γ on either side of the codimension-two point at $\Gamma^* = 1.64$ and $Re^* = 330$. Dots indicate the intersection of these trajectories with various bifurcation curves, identified by the labels. Lines $M(\mu_1 = 0)$ and $P(\mu_2 = 0)$ indicate the locus of steady bifurcations from the axisymmetric state, with $m = 1$ and $m = 2$, respectively. Other curves indicate bifurcations to travelling waves (TW), modulated travelling waves (H), and between different steady states (MP). Heteroclinic orbits exist between the two MP bifurcations. Time-dependent behaviour occurs in a large region of parameter space when M is traversed before P ($\Gamma > \Gamma^*$, solid trajectory), but only extremely near the codimension-two point when the order is reversed ($\Gamma < \Gamma^*$). No time-dependent behaviour occurs along the dashed trajectory.

4.3. *No 1 : 2 mode interaction at* $\Gamma = 1.5$

The neutral curves of figure 2 determine the codimension-two point where the modes $m = 1$ and $m = 2$ bifurcate simultaneously at $(\Gamma^*, Re^*) = (1.64, 330)$. Near this point, the dynamics are described by the normal form (Armbruster, Guckenheimer & Holmes 1988; Proctor & Jones 1988):

$$\dot{z}_1 = \overline{z_1} z_2 + z_1(\mu_1 + e_{11}|z_1|^2 + e_{12}|z_2|^2), \tag{4.2a}$$

$$\dot{z}_2 = \pm z_1^2 + z_2(\mu_2 + e_{21}|z_1|^2 + e_{22}|z_2|^2), \tag{4.2b}$$

where z_1 and z_2 are complex amplitudes of the $m = 1$ and $m = 2$ modes. In a previous paper (Nore *et al.* 2003), we have studied the dynamics at $\Gamma = 2$, where the mode $m = 1$ bifurcates from the basic state before the mode $m = 2$. The two modes interact nonlinearly to create various complex flows as the Reynolds number is increased, such as stationary states with $m = 1$ and $m = 2$, travelling waves, and near-heteroclinic cycles.

We now wish to investigate the nonlinear states which result when the order of the bifurcations is reversed. We thus choose for more detailed study the value $\Gamma = 1.5 < \Gamma^*$ at which the mode $m = 2$ bifurcates linearly at $Re_C = 309$ before the mode $m = 1$ at $Re_{m=1} = 331$. We have used the fully nonlinear version of the code described in § 3.3 to compute nonlinear steady states with increasing Re. We obtain only the branch of $m = 2$ steady states emanating from the supercritical pitchfork at Re_C. Attempts to produce behaviour other than this by initializing the code with odd wavenumber components have not succeeded. It is only for $Re > 900$, far from the codimension-two point at $Re^* = 330$, that the $m = 2$ branch undergoes an instability to an $m = 1$ eigenvector and begins to show a change in spatial and temporal behaviour. In contrast, Mercader, Prat & Knobloch (2002) observe near-heteroclinic cycles in their study of two-dimensional Rayleigh–Bénard convection with different boundary conditions at the top and bottom, for parameter values on either side of the 1 : 2 codimension-two point.

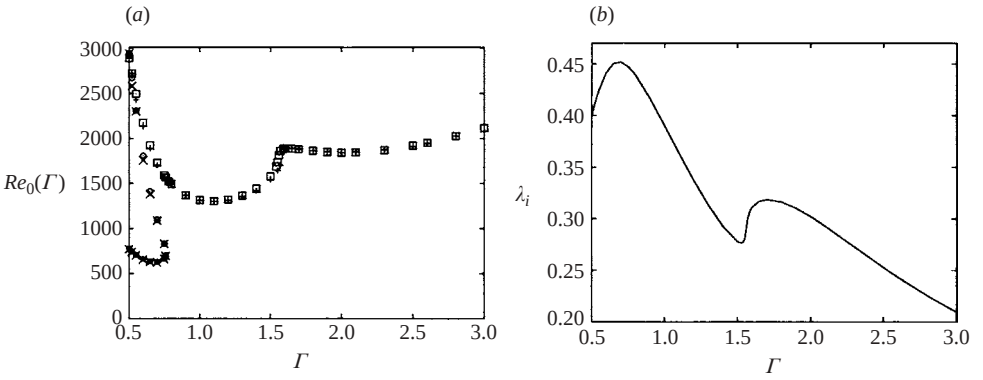

FIGURE 10. (*a*) Comparison of axisymmetric thresholds obtained with coarse and fine resolution. Pitchfork bifurcations P_1, P_2 are indicated by ●, ○, × and Hopf bifurcations H_1 by □, +. Points ×, + are computed with $N_r = 100$, $N_z = 64$ for $\Gamma < 1$ and $N_r = 64$, $N_z = 100$ for $\Gamma \geqslant 1$ while ●, ○, □ are found using ARPACK with $N_r = 200$, $N_z = 128$ for $\Gamma < 1$ and $N_r = 128$, $N_z = 200$ for $\Gamma \geqslant 1$. (*b*) Frequency $\lambda_i(m = 0, Re_0(\Gamma), \Gamma)$ of H_1 at threshold.

These results are consistent with figure 9 where complex behaviour occurs almost exclusively in the $\mu_1 > 0$, $\mu_2 > 0$ quadrant and would be found only extremely near the codimension-two point when the $m = 2$ precedes the $m = 1$ instability. The coefficients $e_{11} = -9$, $e_{12} = -6$, $e_{21} = -5$ and $e_{22} = -5$ of normal form (4.2) used in calculating figure 9 were chosen by J. Porter (personal communication) because they lead to a sequence of bifurcations in qualitative agreement with the numerical results in Nore *et al.* (2003). These coefficients are apparently quite different from those pertaining to the Rayleigh–Bénard convection study of Mercader *et al.* (2002).

5. Axisymmetric linear modes

Although the critical mode is never axisymmetric in the aspect ratio interval under consideration, our goal is to provide a complete survey of linear thresholds, which can be connected continously to other ranges of Γ and s, where axisymmetric modes may become critical. For example, experimental results by Schouveiler *et al.* (1998, 2001) and Gauthier *et al.* (1999) show that, for small Γ, the bifurcation at threshold is to a system of concentric rolls.

Figure 10(*a*) represents the axisymmetric thresholds $Re_0(\Gamma)$ as a function of Γ obtained with a coarse and a fine resolution. This figure and the enlargements of figure 11 show up to four thresholds for each value of Γ. A Hopf bifurcation, denoted by H_1, exists throughout the range $0.5 \leqslant \Gamma \leqslant 3.0$ that we have studied. Two pitchfork bifurcations, denoted by P_1 and P_2, exist for $0.50 \leqslant \Gamma < 0.78$, merging and disappearing at $\Gamma = 0.78$, $Re = 700$. Finally, another Hopf bifurcation, H_2, exists for $0.50 \leqslant \Gamma \leqslant 0.55$, and is annihilated when it meets P_2 at $\Gamma = 0.55$, $Re = 2309$. The termination of the H_2 curve is a Takens–Bogdanov codimension-two bifurcation point, at which the frequency of H_2 goes to zero, as shown in figure 11(*c*).

This complicated evolution can be understood by plotting the growth rates $\lambda_r(m = 0, Re, \Gamma)$ as a function of Re for different aspect ratios Γ, as shown in figure 12. Up to four leading $m = 0$ eigenvalues computed using ARPACK (Lehoucq *et al.* 1998) are represented in figure 12. For lower values of Re, the two leading eigenvalues are real; their intersections with the real axis when $\Gamma < 0.78$ are responsible for the steady bifurcations P_1 and P_2. These eigenvalues collide to form a complex conjugate pair whose real part is plotted on figure 12 and intersects the real axis when $\Gamma < 0.55$,

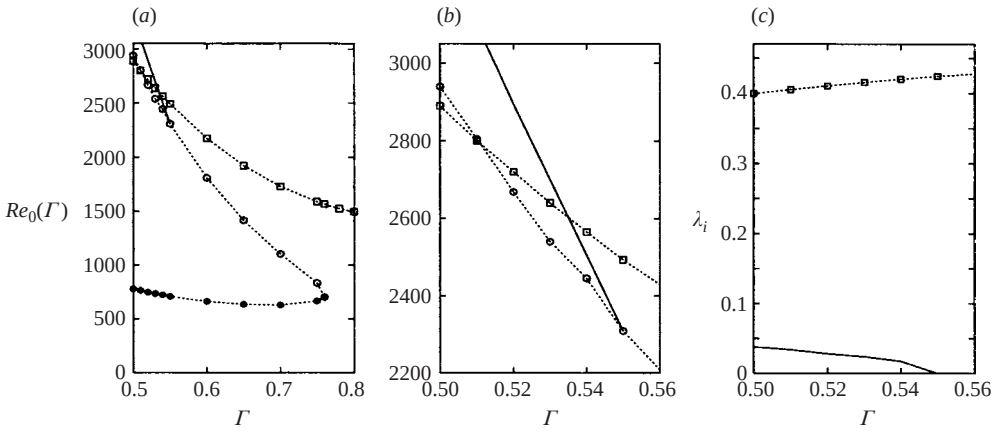

FIGURE 11. (*a*) Axisymmetric thresholds: two stationary bifurcations P_1 (●) and P_2 (○) and two Hopf bifurcations H_1 (□) and H_2 (—). P_1 and P_2 disappear at the isolation formation point at $\Gamma = 0.78$. (*b*) Enlargement of (a) showing the disappearance of H_2 at the Takens-Bogdanov point at $\Gamma = 0.55$. (*c*) Frequencies for H_1 (□) and H_2 (—).

leading to the Hopf bifurcation H_2. Another unrelated complex conjugate pair is also shown on figure 12. Its real part overtakes that of the other eigenvalues for higher Re and intersects the real axis for all Γ values studied, leading to the Hopf bifurcation H_1. The imaginary part of the H_1 pair is different from those of the other eigenvalues (except at $\Gamma = 1.59$; see below), and hence the crossings seen on figure 12 do not correspond to actual intersections of this pair with other eigenvalues.

In figure 13, streamfunction contours of the basic state and of the leading eigenvectors are plotted for the aspect ratio $\Gamma = 0.52$ for Reynolds numbers near thresholds, at the parameter values indicated by vertical lines on figure 12(*d*). The first two rows show real eigenvectors, the third and fourth rows complex eigenvectors. The basic state $\Psi(r, z)$ is symmetric under R_π, while all eigenvectors $\psi(r, z)$ are antisymmetric. At $Re = 760$, near the P_1 bifurcation, the leading eigenvector (figure 13*b*) contains one large cell while the second leading eigenvector (figure 13*c*) also contains a second counter-rotating cell. In the second row, near the P_2 bifurcation, the two leading eigenvectors (figure 13*e*, *f*) resemble one another, containing two counter-rotating regions separated by a curved contour. This resemblance between these two eigenvectors is to be expected, since the Reynolds number $Re = 2660$ is near that at which the real eigenvalues merge to form a complex pair (see figure 12*d*). The third and fourth rows of figure 13 show the basic state and real and imaginary components of the eigenvector responsible for the Hopf bifurcations H_2 and H_1. The H_2 eigenvector component shown in figure 13(*h*) resembles the real eigenvectors (figure 13*e*, *f*) and its magnitude is much larger than that of the component shown in figure 13(*i*). The H_1 eigenvector components (figure 13*k*, *l*) look quite different.

We now examine the axisymmetric threshold at higher values of Γ. Figure 10(*a*) shows that $Re_0(\Gamma)$ presents a rapid increase with Γ for $\Gamma \lesssim 1.6$, while it remains almost constant for $\Gamma \gtrsim 1.6$, with a corresponding variation in the frequency $\lambda_i(m = 0, Re_0, \Gamma)$ at threshold. We have determined that this behaviour is due to the crossing of the two leading eigenvalues, both complex. The intersection of complex eigenvalues, unlike that of real eigenvalues, is a codimension-two phenomenon: both Γ and Re must be adjusted in order to make the real and the imaginary parts of the two eigenvalues equal.

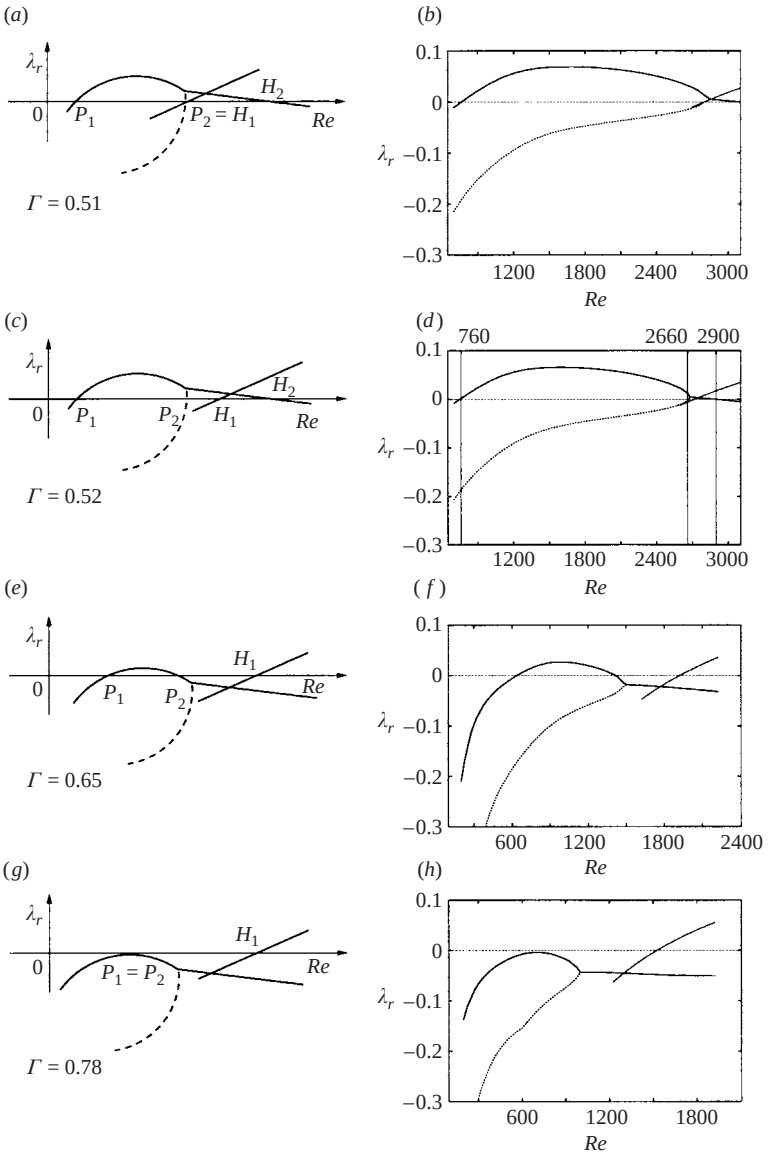

FIGURE 12. Growth rate $\lambda_r(0, Re, \Gamma)$ of the four $m = 0$ leading eigenvalues as a function of Re for different Γ. Left-hand column, schematic diagrams, right-hand column, computed values: (a,b) $\Gamma = 0.51$, (c,d) $\Gamma = 0.52$, (e,f) $\Gamma = 0.65$ and (g,h) $\Gamma = 0.78$. Note that there are two stationary thresholds denoted as P_1 and P_2 for $\Gamma < 0.78$. These eigenvalues collide to form a complex conjugate pair whose real part is plotted and intersects the real axis when $\Gamma < 0.55$, leading to the Hopf bifurcation H_2. Another unrelated complex conjugate pair leads to another Hopf bifurcation H_1 for $0.5 \leqslant \Gamma \leqslant 3$. Its imaginary part differs from those of the other eigenvalue branches, so the apparent intersections are not genuine, but rather an artefact of the projection onto the λ_r-axis.

Figure 14 shows the evolution of the two leading eigenvalues in the (λ_r, λ_i)-plane as Re is varied, for four different values of Γ. For $\Gamma = 1.55$, one eigenvalue branch extends across the diagram: the real part λ_r increases monotonically with Re, becoming positive at the H_1 bifurcation at $Re_0(1.55) = 1737$. A second branch,

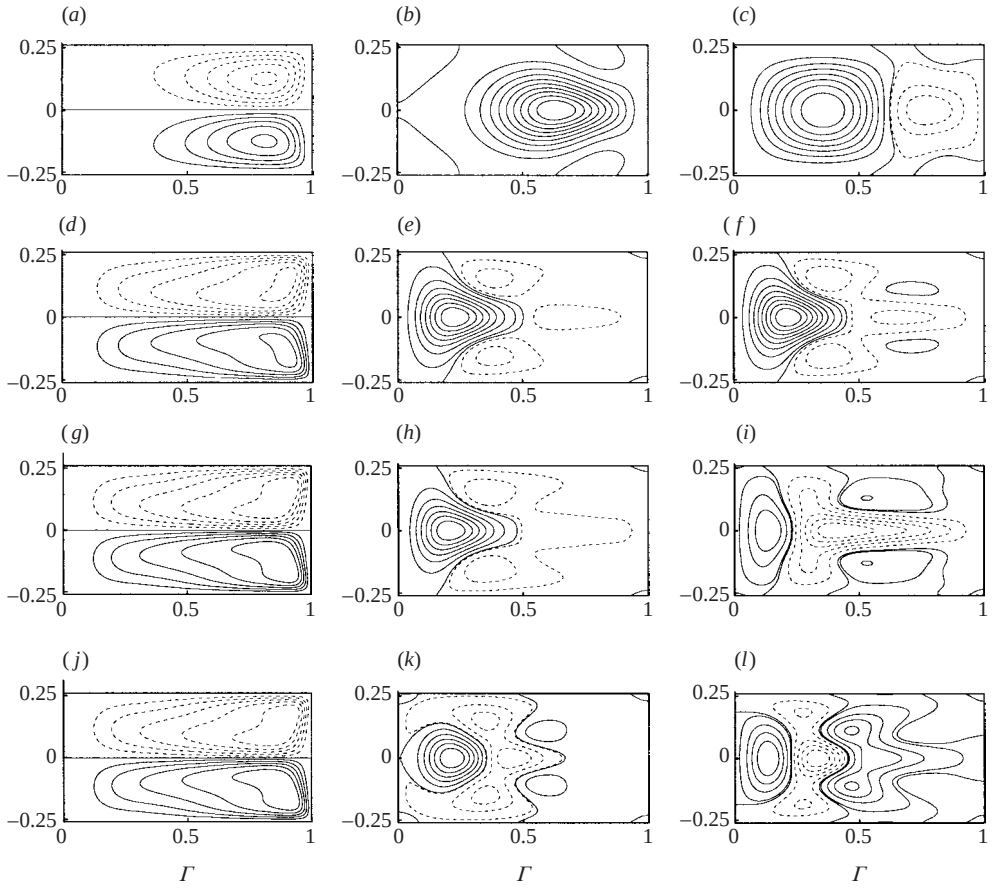

FIGURE 13. Streamfunction contours of axisymmetric states for $\Gamma = 0.52$. In the first row, $Re = 760$, near bifurcation P_1: (*a*) basic state; (*b*) the leading eigenvector responsible for the P_1 bifurcation; (*c*) the second leading eigenvector. On the second row, $Re = 2660$, near bifurcation P_2: (*d*) basic state; (*e*) the leading eigenvector; (*f*) the second leading eigenvector responsible for the P_2 bifurcation. On the third and fourth rows, $Re = 2900$: (*g*) basic state; (*h*, *i*) real and imaginary parts of the leading eigenpair responsible for the Hopf bifurcation H_2; (*j*) basic state; (*k*, *l*) real and imaginary parts of the leading eigenpair responsible for the Hopf bifurcation H_1. See figure 12 (*c*, *d*) for this aspect ratio. Positive (negative) values are indicated by solid (dashed) curves.

with a higher λ_i, forms a loop at the left of the diagram, with a local maximum near $\lambda_r \approx -0.04$. By $\Gamma = 1.58$, the bifurcating eigenvalue branch has become folded into an S shape; an increasing portion of the branch is drawn into the $\lambda_r < 0$ half-plane, postponing the H_1 bifurcation to higher values of Re and of λ_i. At $\Gamma = 1.59$, the second eigenvalue branch joins with the first. Inspection of the eigenvectors corresponding to the two leading eigenvalues for $\Gamma = 1.59$ and $Re = 1880$ leads to the conclusion that the two eigenvectors are identical at the crossing. This reconnection leads to the discontinuities in the derivatives of the threshold and frequency curves in figure 10. The curves seen in figure 14 illustrate the way in which the roots of a cubic polynomial cross one another as the coefficients of the polynomial are varied. (This evolution is familiar in the dynamical-systems context from the unfolding of a transcritical bifurcation.) All the codimension-two points involving the axisymmetric modes are given in table 4.

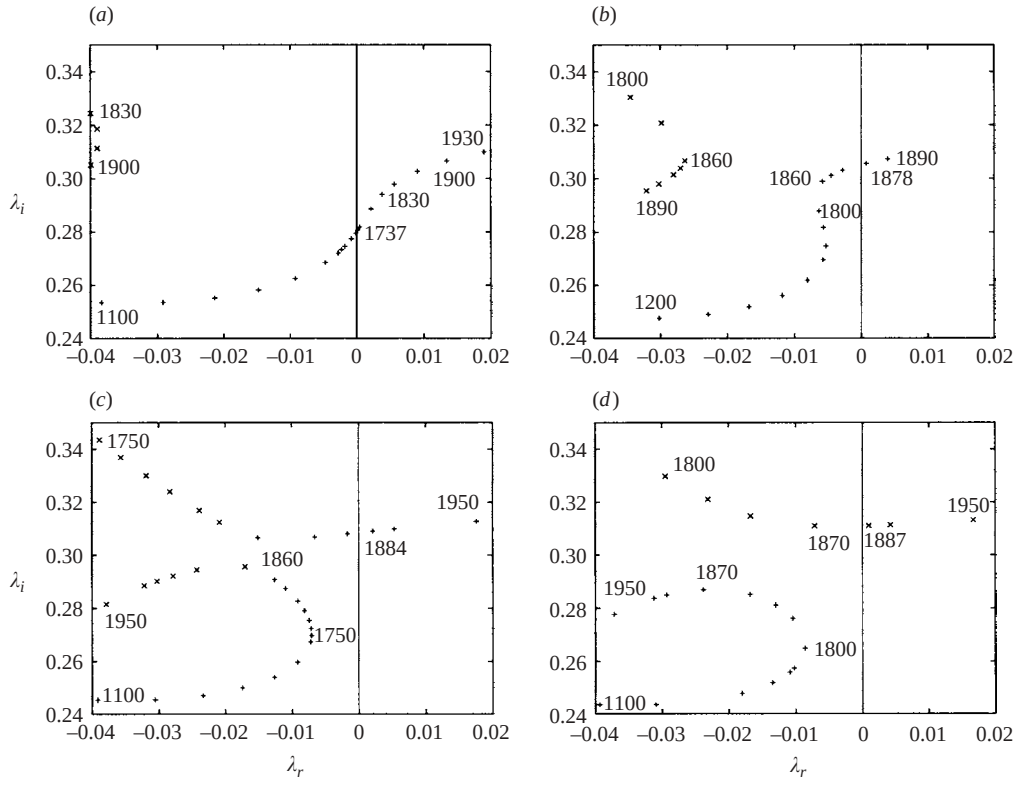

FIGURE 14. Real and imaginary parts of the two leading eigenvalues playing a role in the H_1 Hopf bifurcation: (*a*) $\Gamma = 1.55$, (*b*) $\Gamma = 1.58$, (*c*) $\Gamma = 1.59$, (*d*) $\Gamma = 1.6$. The vertical line $\lambda_r = 0$ defines the bifurcation threshold with $\lambda_r = 0$: $Re_0(1.55) = 1737$, $Re_0(1.58) = 1878$, $Re_0(1.59) = 1884$ and $Re_0(1.6) = 1887$.

Bifurcations	Γ	Re	Description
H_1/P_2	0.51	2802	
H_1/H_2	0.535	2602	
H_2/P_2	0.55	2309	Takens–Bogdanov point
P_1/P_2	0.78	700	Isola formation point
H_1	1.59	1860	Intersection of two complex eigenvalues

TABLE 4. Axisymmetric codimension-two points.

The nearly vertical tangent of the threshold curve near $\Gamma = 1.6$ in figure 10(*a*) explains the discrepancy between our thresholds and those of Gelfgat *et al.* (1996) (see § 3.4). Figure 10(*a*) compares the axisymmetric thresholds $Re_0(\Gamma)$ obtained with a coarse and a fine resolution. The largest difference between the two resolutions, 8.6%, occurs near $\Gamma = 1.6$, where the variation of the Hopf thresholds is greatest. This is because $\Delta Re/\Delta\Gamma \to \infty$ for $\Gamma \sim 1.6$; a consequence of this is that for a fixed aspect ratio, the thresholds between the two resolutions can differ by an $O(1)$ value. Conversely, the variation of Γ with Reynolds number is such that $\Delta\Gamma/\Delta Re \to 0$. Indeed, when figure 10(*a*) is interpreted as describing a function $\Gamma_C(Re)$, i.e. when the differences are taken horizontally rather than vertically, the results from the two

resolutions agree to within 1.8% in Γ. Similar conclusions apply near $\Gamma = 0.5$, where the threshold also varies rapidly. Consequently, figure 10(*a*) shows that the spatial resolution we have used is adequate.

6. Conclusion

We have determined the linear three-dimensional instabilities of the flow between exactly counter-rotating disks over the aspect ratio range $\Gamma = H/R \in [0.5, 3]$ with azimuthal wavenumber $m \leqslant 5$. The dynamics are dominated by the instability of the equatorial shear layer following the physical mechanism of the Kelvin–Helmholtz instability. The roll-up of the shear layer gives rise to stationary radial vortices along the static periphery. We have determined the critical azimuthal wavenumber corresponding to each value of Γ and established the approximate law $m_C \sim 2.2/\Gamma$: the greater the non-dimensional radius, the greater the number of vortices formed. This is consistent with the simple rule that each vortex occupies half of the cylinder height.

The stationarity of the vortices is a consequence of the symmetry of the configuration and of the basic flow: the rotation speeds of the upper and lower disks are equal and opposite. This makes the system invariant under rotation by π about any horizontal axis, as well as any rotation about the vertical axis, leading to the symmetry group $O(2)$. An experiment using a water–glycerol mixture is planned to check our predictions. Any experimental imperfection will break the R_π invariance, thus leaving only the $SO(2)$ group of rotations about the vertical axis, which leads generically to rotating patterns (Knobloch 1993). Our challenge will be to obtain experimentally stationary vortices and to study the shape of these axisymmetry-breaking structures.

We have located the 1 : 2 codimension-two point at which the $m = 1$ and $m = 2$ thresholds coincide as $\Gamma^* = 1.64$ and $Re^* = 330$. In a previous paper (Nore *et al.* 2003), we studied the sequence of nonlinear states which occur as Re is varied near this codimension-two point for $\Gamma = 2$, where the $m = 1$ threshold precedes that of $m = 2$. These states included travelling waves and robust heteroclinic cycles. For $\Gamma = 1.5$, where the $m = 2$ threshold precedes that of $m = 1$, no such states occur.

For $0.5 \leqslant \Gamma \leqslant 3$, the first instability is never axisymmetric; we have nevertheless computed $m = 0$ thresholds for completeness and in the hope of connecting these to primary axisymmetric instabilities at other parameter values. The sequence of axisymmetric instabilities is complicated, involving a pair of pitchfork bifurcations and two Hopf bifurcations, which succeed one another via various codimension-two points. Over most of the range studied, there exists only one axisymmetric instability, a Hopf bifurcation, the steep variation of whose threshold with Γ poses theoretical and numerical challenges.

We gratefully acknowledge Yann Fraigneau for his technical assistance, Alexander Gelfgat for providing his results reported in table 1 and Dwight Barkley for helpful discussions. The computations were carried out on the NEC-SX5 computer of the Institut du Développement et des Ressources en Informatique Scientifique (IDRIS) of the Centre National pour la Recherche Scientifique (CNRS) (project 0254).

REFERENCES

Armbruster, D., Guckenheimer, J. & Holmes, P. 1988 Heteroclinic cycles and modulated traveling waves in systems with O(2) symmetry. *Physica* D **29**, 257–282.

Barbosa, E. & Daube, O. 2002 A finite differences method in cylindrical coordinates for 3D incompressible flows. *Computers & Fluids* (in press).

Batchelor, G. K. 1951 Note on a class of solutions of the Navier–Stokes equations representing steady rotationally-symmetric flow. *Q. J. Mech. Appl. Maths* **4**, 29–41.

Betchov, R. & Szewczyk, A. 1963 Stability of a shear layer between parallel streams. *Phys. Fluids* **6**, 1391–1396.

Blackburn, H. M. & Lopez, J. M. 2000 Symmetry breaking of the flow in a cylinder driven by a rotating end wall. *Phys. Fluids* **12**, 2698–2701.

Blackburn, H. M. & Lopez, J. M. 2002 Modulated rotating waves in an enclosed swirling flow. *J. Fluid Mech.* **465**, 33–58.

Cousin-Rittemard, N., Daube, O. & Le Quéré, P. 1998 Sur la nature de la première bifurcation des écoulements interdisques. *C. R. Acad. Sci. Paris* **326**, 359–366.

Daube, O. & Le Quéré, P. 2002 Numerical investigation of the first bifurcation for the flow in a rotor–stator cavity of radial aspect ratio 10. *Computers & Fluids* **31**, 481–494.

Faller, A. J. 1991 Instability and transition of disturbed flow over a rotating disk. *J. Fluid Mech.* **230**, 245–269.

Gadoin, E., Le Quéré, P. & Daube, O. 2001 A general methodology to investigate flow instabilities in complex geometries : application to natural convection in enclosures. *Intl J. Numer. Meth. Fluids* **37**, 175–208.

Gauthier, G., Gondret, P., Moisy, F. & Rabaud, M. 2002 Instabilities of the flow between co and counter–rotating disks. *J. Fluid Mech.* **473**, 1–21.

Gauthier, G., Gondret, P. & Rabaud, M. 1999 Axisymmetric propagating vortices in the flow between a stationary and a rotating disk enclosed by a cylinder. *J. Fluid Mech.* **386**, 105–126.

Gelfgat, Y. A., Bar-Yoseph, P. Z. & Solan, A. 1996 Steady states and oscillatory instability of swirling flow in a cylinder with rotating top and bottom. *Phys. Fluids* **8**, 2614–2625.

Gelfgat, Y. A., Bar-Yoseph, P. Z. & Solan, A. 2001 Three-dimensional instability of axisymmetric flow in a rotating lid–cylinder enclosure. *J. Fluid Mech.* **438**, 363–377.

Goda, K. 1979 A multistep technique with implicit difference schemes for calculating two- or three-dimensional cavity flows. *J. Comput. Phys.* **30**, 76–95.

Hyman, J. M. & Shashkov, M. 1997 Natural discretizations for the divergence, gradient and curl on logically rectangular grids. *Comput. Maths Applic.* **33**, 81–104.

von Kármán, T. 1921 Über laminare und turbulente Reibung. *Z. Angew. Math. Mech.* **1**, 233–252.

Knobloch, E. 1993 Bifurcations in rotating systems. In *Theory of Solar and Planetary Dynamos: Introductory Lectures* (ed. M. R. E. Proctor & A. D. Gilbert). Cambridge University Press.

Lehoucq, R. B., Sorensen, D. C. & Yang, C. 1998 *ARPACK User's Guide, Philadelphia.* SIAM, Philadelphia.

Lopez, J. M., Marques, F. & Sanchez, J. 2001 Oscillatory modes in an enclosed swirling flow. *J. Fluid Mech.* **439**, 109–129.

Lopez, J. M., Hart, J. E., Marques, F., Kittelman, S. & Shen, J. 2002 Instability and mode interactions in a differentially–driven rotating cylinder. *J. Fluid Mech.* **462**, 383–409.

Mamun, C. K. & Tuckerman, L. S. 1995 Asymmetry and Hopf bifurcation in spherical Couette flow. *Phys. Fluids* **7**, 80–91.

Mercader, I., Prat, J. & Knobloch, E. 2002 Robust heteroclinic cycles in two-dimensional Rayleigh–Bénard convection without Boussinesq symmetry. *Intl J. Bif. Chaos* **12**, 2501–2522.

Moisy, F., Doaré, O., Pasutto, T., Daube, O. & Rabaud, M. 2003 Experimental and numerical study of the shear layer instability between two counter-rotating disks. *J. Fluid Mech.* **507**, 175–202

Nore, C., Tuckerman, L. S., Daube, O. & Xin, S. 2003 The 1:2 mode interaction in exactly counter-rotating von Kármán swirling flow. *J. Fluid Mech.* **477**, 51–88.

Pikhtov, S. V. & Smirnov, E. M. 1993 Boundary layer stability on a rotating disk with corotation of the surrounding fluid. *Fluid. Dyn.* **27**, 657–663.

Proctor, M. R. E. & Jones, C. A. 1988 The interaction of two spatially resonant patterns in thermal convection. Part 1. Exact 1:2 resonance *J. Fluid Mech.* **188**, 301–335.

Saad, Y. & Schultz, M. H. 1986 GMRES: a generalized minimal residual algorithm for solving nonsymmetric linear systems. *SIAM J. Sci. Stat. Comput.* **7**, 856–869.

Schouveiler, L., Le Gal, P. & Chauve, M.-P. 1998 Stability of a traveling roll system in a rotating disk flow. *Phys. Fluids* **10**, 2695–2697.

Schouveiler, L., Le Gal, P. & Chauve, M.-P. 2001 Instabilities of the flow between a rotating and a stationary disk. *J. Fluid Mech.* **443**, 329–350.

Serre, E., Crespo del Arco, E. & Bontoux, P. 2001 Annular and spiral patterns in flows between rotating and stationary disks. *J. Fluid Mech.* **434**, 65–100.

Sorensen, D. C. 1992 Implicit Application of Polynomial Filters in a k-Step Arnoldi Method. *SIAM* **13**, 357–385.

Sotiropoulos, F. & Ventikos, Y. 1998 Transition from bubble–type vortex breakdown to columnar vortex in a confined swirling flow. *Intl J. Heat Fluid Flow* **19**, 446–458.

Sotiropoulos, F. & Ventikos, Y. 2001 The three-dimensional structure of confined swirling flows with vortex breakdown. *J. Fluid Mech.* **426**, 155–175.

Spohn, A., Mory, M. & Hopfinger, E. J. 1998 Experiments on vortex breakdown in a confined flow generated by a rotating disk. *J. Fluid Mech.* **370**, 73–99.

Tuckerman, L. S. 1989 *Steady-state solving via Stokes preconditioning: recurrence relations for elliptic operators.* (ed. D. L. Dwoyer, M. Y. Hussaini & R. G. Voigt). Springer.

Zandbergen, P. J. & Dijkstra, D. 1987 Von Kármán swirling flows. *Annu. Rev. Fluid Mech.* **19**, 465–491.